UC Berkeley

UC Berkeley Previously Published Works

Title

Theoretical Study of 4-(Hydroxymethyl)benzoic Acid Synthesis from Ethylene and 5-(Hydroxymethyl)furoic Acid Catalyzed by Sn-BEA

Permalink

https://escholarship.org/uc/item/2g0669g1

Journal

ACS Catalysis, 6(8)

ISSN

2155-5435

Authors

Li, Yi-Pei
Head-Gordon, Martin
Bell, Alexis T

Publication Date

2016-08-05

DOI

10.1021/acscatal.6b01160

Peer reviewed

eScholarship.org Powered by the California Digital Library
University of California

ACS Catalysis

Research Article

pubs.acs.org/acscatalysis

Theoretical Study of 4-(Hydroxymethyl)benzoic Acid Synthesis from Ethylene and 5-(Hydroxymethyl)furoic Acid Catalyzed by Sn-BEA

Yi-Pei Li,[†] Martin Head-Gordon,[‡] and Alexis T. Bell*[,†]

[†]Department of Chemical and Biomolecular Engineering, University of California, Berkeley, California 94720-1462, United States
[‡]Department of Chemistry, University of California, Berkeley, California 94720-1462, United States

Supporting Information

ABSTRACT: A sustainable route has been reported for the production of terephthalic acid (PTA) from 5-(hydroxymethyl)furoic acid (HMFA) and ethylene, both of which can be derived from biomass. This process starts with the production of 4-(hydroxymethyl)benzoic acid (HMBA) from HMFA and ethylene catalyzed by Sn-BEA. The subsequent oxidation of HMBA leads to PTA. The present study reports the results of a detailed computational investigation of the mechanism of HMBA synthesis from ethylene and HMFA mediated by Sn-BEA. Density functional theory calculations show that the formation of HMBA proceeds via Diels–Alder cycloaddition of HMFA and ethylene, which is rate-limiting, followed by Lewis acid-catalyzed dehydration. The solution-phase reaction and six different pathways in Sn-BEA, including one pathway on the Si site and five different pathways on the Sn site, are investigated for the Diels–Alder cycloaddition of HMFA and ethylene. Energy decomposition analysis (EDA) shows that the Sn site stabilizes the transition state of the Diels–Alder reaction electrostatically instead of facilitating charge transfer between HMFA and ethylene. Therefore, the preferred pathway for the Diels–Alder reaction starts with binding HMFA to the Sn site by the carbonyl oxygen, which is the configuration that maximizes electrostatic interactions between substrates and the catalyst in the transition state. The effect of substituting Sn in the active site by Zr and Ti was examined and the highest reaction barriers were for the Ti sites. Using EDA, we found that though the barriers of the Sn and Zr site are comparable, the individual contributing effects are different: lower energy penalty associated with distortion of the geometry of the Zr site overcomes less favorable electrostatic and charge transfer effects compared to the Sn site.

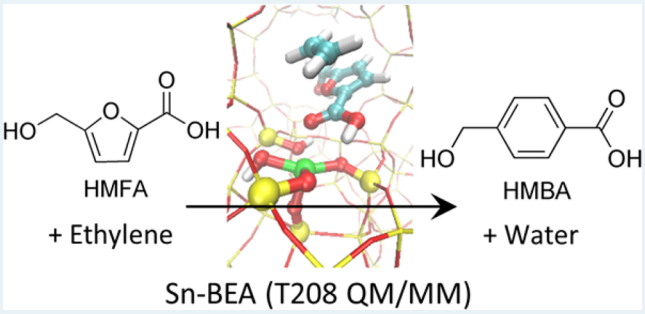

KEYWORDS: *quantum mechanics-molecular mechanics, energy decomposition analysis, zeolite, Diels–Alder, catalysis, reaction mechanism*

Downloaded via UNIV OF CALIFORNIA BERKELEY on June 22, 2018 at 00:32:04 (UTC).
See https://pubs.acs.org/sharingguidelines for options on how to legitimately share published articles.

INTRODUCTION

Terephthalic acid (PTA) is one of the monomers used in the production of polyethylene terephthalate (PET) and is produced conventionally by the oxidation of *p*-xylene derived from petroleum. Increasing global demand for PET together with the desire to replace petroleum-based chemicals has stimulated the consideration of routes to PTA from renewable carbon sources, such as biomass.[1] One approach to *p*-xylene formation that has been considered is Diels–Alder cycloaddition of 2,5-dimethylfuran (DMF) and ethylene followed by dehydration of the resulting product, because both starting materials can be produced from biomass—ethylene by dehydration of bioethanol and DMF by hydrodeoxygenation of 5-hydroxymethylfurfural (HMF).[2−4] However, economic analysis has revealed that the cost of *p*-xylene derived from DMF and ethylene is higher than that derived from petroleum.[5] Recently, Pacheco and Davis pointed out that because the end product, PTA, is the fully oxidized variant of *p*-xylene, the cost of PTA derived from HMF could be reduced if the intermediate, *p*-xylene, is replaced by oxidized variants of *p*-xylene (see Scheme 1) because in this case the reduction of HMF to DMF, which requires a hydrogen source, can be eliminated.[6] It was reported that this strategy can be achieved by partially oxidizing HMF to 5-(hydroxymethyl)furoic acid (HMFA) and then reacting this product with ethylene via Diels–Alder cycloaddition, as shown in Scheme 1. Subsequent dehydration of the Diels–Alder product results in 4-(hydroxymethyl)benzoic acid (HMBA), an oxidized variant of *p*-xylene that can be easily converted to PTA.[6]

The production of *p*-xylene from DMF and ethylene is similar to the production of HMBA from HMFA and ethylene in that both processes proceed by way of a Diels–Alder cycloaddition followed by dehydration of the Diels–Alder adduct. We have recently addressed the question of how a Brønsted acid zeolite catalyzes the production of *p*-xylene from DMF and ethylene through a detailed theoretical analysis of the

Received: April 24, 2016
Revised: June 10, 2016
Published: June 23, 2016

© 2016 American Chemical Society

DOI: 10.1021/acscatal.6b01160
ACS Catal. 2016, 6, 5052−5061

Scheme 1. Schematic Representations of Two Pathways for Conversion of Hydroxymethylfurfural (HMF) to Terephthalic Acid (PTA)[a]

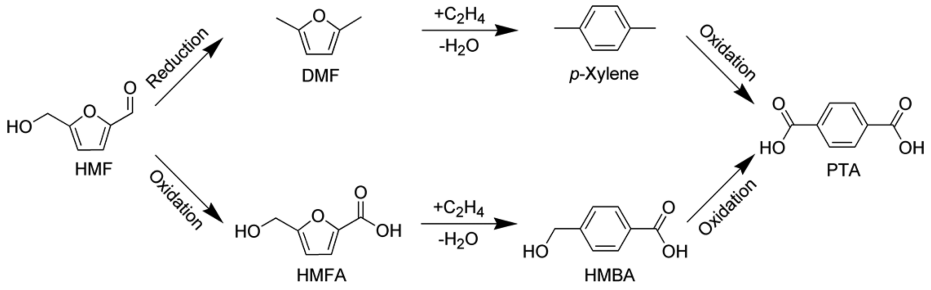

[a]This paper focuses on the lower pathway, which avoids the need for initial reduction of HMF, and the associated hydrogen source.

reaction pathway.[7] However, because the production of HMBA from HMFA and ethylene is catalyzed by Sn-BEA, a Lewis acid zeolite, the mechanism is expected to be very different from the Brønsted acid pathway. Here we report a detailed analysis of the mechanism for the synthesis of HMBA from HMFA and ethylene mediated by Sn-BEA. The kinetic analysis of the preferred mechanism suggests that Diels–Alder cycloaddition is the rate-limiting step.

A further question that we have addressed is the role of Sn-BEA on the Diels–Alder cycloaddition process. Energy decomposition analysis (EDA)[8] reveals that Sn-BEA stabilizes the Diels–Alder transition state through electrostatic interactions between the substrates and the catalyst instead of directly facilitating electron transfer between HMFA and ethylene. The magnitude of electrostatic interactions correlates well with the dipole moment of the substrate which directly interacts with the active site in the transition state so that the configurations in which HMFA, instead of ethylene, binds directly to the site are preferred for Diels–Alder cycloaddition of HMFA and ethylene. We have also investigated the activities of zeolites containing Zr and Ti at the active site instead of Sn. The lowest reaction barriers are for Sn and Zr sites in good agreement with the experimental observation that the activities for Sn-BEA and Zr-BEA are comparable and both are higher than that of Ti-BEA.[6] Using EDA, we find that the Sn site can strongly stabilize the transition state through electrostatic and charge transfer interactions because central atom of the site carries high positive charges. On the other hand, because Zr is highly polarizable, the Zr site has low energy penalties associated with geometric distortion from its resting geometry to the geometry in the transition state. Therefore, though the reaction barriers for Sn and Zr sites are comparable, the individual contributing factors are different.

THEORETICAL METHODS

Zeolite Model Geometries. The structure of Sn-BEA has been thoroughly investigated previously. It has been shown that the catalytic activity of Sn-BEA is critically dependent on the successful incorporation of Sn into the zeolite framework and that framework Sn sites exhibit unique adsorption properties that differ from those for nonframework SnO_2.[9,10] Moreover, two types of framework Sn sites have been identified: one is the fully coordinated Sn site (closed site), the other is the partially hydrolyzed Sn site (open site).[11,12] Since the open site has been shown to be more active than the closed site because of the extra flexibility provided by the defect in the lattice,[11,13−15] our model of Sn-BEA was made by replacing a Si atom in the framework by a Sn atom with one of the Sn−O−Si bridges replaced by Sn−OH and Si−OH, as shown in Figure 1. For this study, we considered the Sn atom to be in the T2 site in the

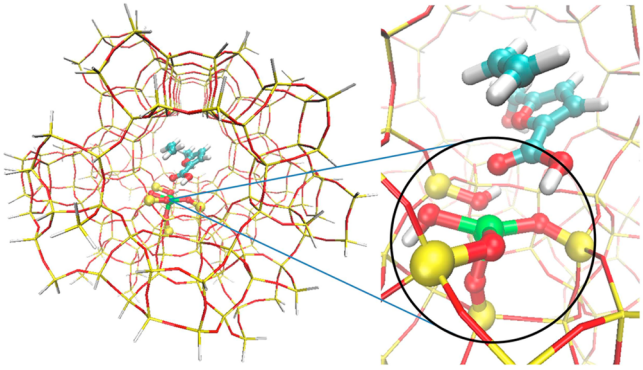

Figure 1. Sn-BEA QM/MM model (T208), where the T2 site is shown. Atoms shown in cyan, white, red, yellow, and green represent C, H, O, Si, and Sn atoms, respectively. Spherical atoms are QM atoms, others are MM atoms.

nomenclature of Newsam et al.,[16] one of the two sites that are favored for Sn atom substitution among the nine unique T atom positions in BEA.[17,18] The zeolite framework was described by a T208 cluster terminated with hydrogen atoms by replacing the terminal oxygen atoms. The positions of all Si and O atoms are determined by the crystallographic structure of BEA.[16] The procedures used to construct Zr-BEA and Ti-BEA are the same as Sn-BEA because the preferred position for Zr and Ti substitution in BEA is also the T2 site.[19] Though the Lewis acidity of the site can vary between different crystallographic positions,[19] we consider the substitution of Sn, Zr, and Ti in one single position (T2) in this work to compare the effects of different heteroatoms on the reaction.

QM/MM Computations. Implementation of the QM/MM model in this work followed the electrostatic embedding scheme described previously,[20] which has been employed to study reactions and adsorptions in Sn-BEA,[15] H-BEA,[7] and other zeolite systems.[21−27] Because it has been shown previously that the accuracy of large cluster model QM/MM calculations is nearly independent of QM region beyond a T5 region,[22,26] in this work, as shown in Figure 1, only reactants and a T5 cluster encompassing the active center were described by QM, whereas the rest of the zeolite was described by MM (T5 QM/T203 MM). All geometry optimizations were performed by relaxing only the QM region, while keeping all the MM atoms frozen (see Text S1 in Supporting Information for a discussion of whether relaxing the T5 QM region

DOI: 10.1021/acscatal.6b01160
ACS Catal. 2016, 6, 5052−5061

encompassing the site is sufficient to capture the local flexibility of the lattice). The hydrogen terminations of the QM region were kept along each of the terminal Si−O bonds at a distance of 0.92 R(Si−O) from the terminal Si atom.[20]

The atoms of the zeolite cluster in the MM region were described using a standard force field of the CHARMM type,[28−30] for which the parameters are listed in Table 1.[22] The van der Waals radius for O and Si are the standard CHARMM parameters.[30] The charges and the characteristic energies for the Lennard-Jones potential used were selected and validated by reducing the deviation between QM/MM calculations and QM calculations as well as experimental data over a range of adsorption energies and transition states in MFI and H-MFI, and H-BEA.[20,22] Standard CHARMM parameters were used for the atoms of the substrates.[30] The QM region was treated at the ωB97X-D[31,32]/Def2-SV(P) and ωB97X-D/Def2-TZVPD levels of theory for geometry optimizations and single-point energy calculations, respectively. Reaction intermediates were guessed by hand followed by standard geometry optimizations to refine the structures. The structures of transition states connecting intermediates were found by the freezing string method[33] followed by local optimization. All QM and QM/MM calculations were carried out using a development version of the Q-Chem software package.[34] Partial charges on atoms were calculated using natural bond orbital (NBO) analysis.[35] Reported energies and free energies were calculated at experimental temperature (463 K) using a modified rigid rotor-harmonic oscillator model (quasi-RRHO),[22,36] which replaces the contribution of low-lying vibrations by a corresponding rotor with the same frequency. The reference-state concentration chosen for all solutes is 1M. Because the quasi-RRHO model does not account for the translational entropies of the adsorbates in zeolites,[37,38] the estimated entropy loss upon adsorption is likely to be overestimated. Therefore, the reported free energies of the transition states in zeolites with respect to free reactants should be viewed as upper bounds to the true apparent free energy barriers (see Text S2 in Supporting Information for more detailed discussions of this point).

Table 1. Charge and Lennard-Jones Parameters for O and Si Used in the QM/MM Portion of This Work

Q_{Si}	Q_O	ε_{Si} (kcal/mol)	R_{Si} (Å)	ε_O (kcal/mol)	R_O (Å)
0.7	−0.35	0.047	2.2	0.018	1.77

Solvation of Substrates. In order to be consistent with the previously reported experimental conditions,[6] where dioxane was used as the solvent, the energies of the HMFA and ethylene (ET) solvated in dioxane, instead of gas-phase energies, were chosen as the references for the energy surface. Therefore, the energy of state i is written as

$$\begin{aligned} E^i &= E(\mathrm{S{\cdot}C})^i - E(\mathrm{C}) - E_{sol}(\mathrm{HMFA}) - E_{sol}(\mathrm{ET}) \\ &= E(\mathrm{S{\cdot}C})^i - E(\mathrm{C}) - [E(\mathrm{HMFA}) + \Delta E_{sol}(\mathrm{HMFA}) \\ &\quad + E(\mathrm{ET}) + \Delta E_{sol}(\mathrm{ET})] \end{aligned} \quad (1)$$

where $E(\mathrm{S{\cdot}C})^i$ is the energy of the substrate−catalyst complex in state i, $E(\mathrm{C})$ is the energy of the catalyst, $E_{sol}(\mathrm{X})$ is the energy of the solvated substrate X, $E(\mathrm{X})$ is the energy of substrate X in gas phase, and $\Delta E_{sol}(\mathrm{X})$ is the solvation energy of substrate X in dioxane. The solvation energies were estimated using the C-PCM solvation model.[39]

RESULTS AND DISCUSSION

Reaction Mechanism in Sn-BEA. The lowest-energy mechanism in Sn-BEA and the associated potential energy and free energy surfaces for the formation of HMBA from HMFA and ethylene are shown in Figure 2. The mechanism

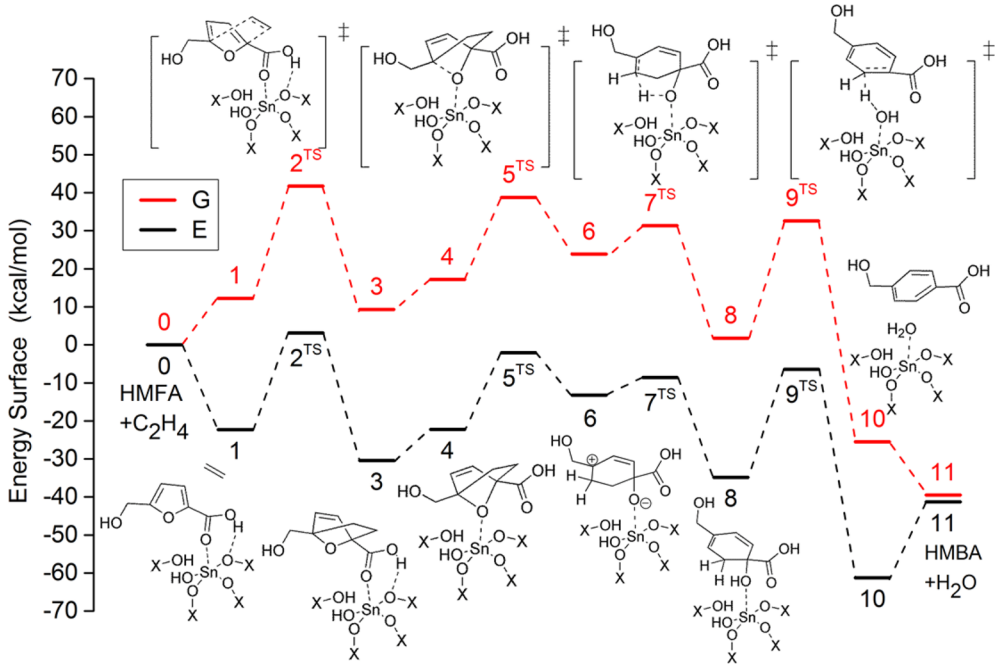

Figure 2. Energy (E) and free energy (G) surfaces for the most favorable path for formation of HMBA from HMFA and ethylene mediated by the T2 site of Sn-BEA. A barrier was not located for states 3 to 4, a step which does not involve covalent bond-making or breaking (and thus is not rate-determining).

DOI: 10.1021/acscatal.6b01160
ACS Catal. 2016, 6, 5052−5061

consists of a Diels–Alder cycloaddition (species **1** to **3**) followed by a Lewis acid catalyzed dehydration (species **4** to **10**). The reaction starts with the binding of HMFA to the active site by coordinating the oxygen atom of the carbonyl group to the Sn center as shown in **1**. This coordination mode was found to be the preferred one for the Diels–Alder cycloaddition between HMFA and ethylene in Sn-BEA. As shown in Figure 3, we have also investigated four other

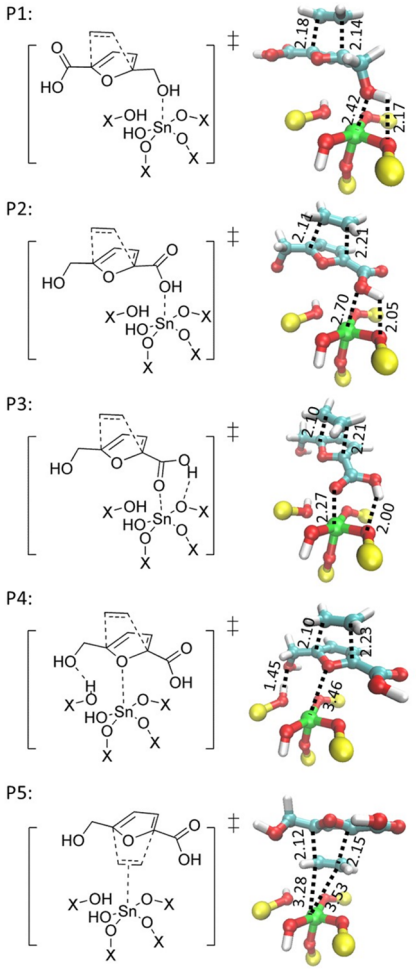

Figure 3. Transition states for five different mechanisms of Diels–Alder cycloaddition of HMFA and ethylene catalyzed by Sn-BEA. Pathway P3 is preferred and was shown as TS-**2** on Figure 2. For clarity, the extended zeolite cluster is not shown. Selected bond lengths are given in Å.

pathways for Diels–Alder cycloaddition of HMFA and ethylene for the Sn site, in addition to carbonyl oxygen coordination of HMFA to Sn (P3). The other pathways involve binding ethylene to the active site (P5), coordinating HMFA to the active site using the hydroxyl oxygen (P1), using the hydroxyl oxygen of the carboxyl group (P2), and using the oxygen atom in the five-membered ring (P4). The energy barriers for these five pathways are tabulated in Table 2. Recent studies show that with Brønsted acid catalysts, condensation of furanic compounds with other species could start with opening of the furan ring by protonation of the double bonds of furan.[40,41] An attempt was made to find a Lewis acid analog by searching pathways starting with binding the conjugated double bonds of HMFA to the Lewis acid center; however, this attempt failed.

Table 2. Apparent Energy Barriers (Energies of Transition States with respect to Solvated Reactants) for Diels–Alder Cycloaddition of HMFA and Ethylene Following Pathways Shown in Figure 3[a]

	P1	P2	P3	P4	P5
E_a (kcal/mol)	4.2	10.0	3.2	5.2	15.9

[a]Free energy barriers are listed in Table S6. The trends of free energy and energy barriers are identical.

Geometry optimizations starting with this configuration led to structures in which one of the oxygen atoms of HMFA coordinates to the Sn atom. To examine whether the Diels–Alder reaction between HMFA and ethylene could occur without the aid of the Sn site, the barriers for the Diels–Alder reaction in Si-BEA and in dioxane were also calculated and are listed in Table 3. These alternative pathways are discussed in detail in the following subsections.

As shown in Figure 2, after the Diels–Alder cycloaddition, the Lewis acid-catalyzed dehydration starts with coordinating the COC bridgehead oxygen atom to the Sn center, state **4**. This coordination promotes the ring-opening of the cycloadduct via transition state TS-**5**. The subsequent proton transfer from the six-membered ring to the oxygen atom coordinating to the Sn center via transition state TS-**7** forms a hydroxyl group and conjugated double bonds on the ring, state **8**. Then, as shown by the transition from state **8** to **10**, water and the end product HMBA are produced by another proton transfer to the hydroxyl group formed in the previous step from the adjacent position. Though the dehydration pathway (states **4** to **10**) shown in Figure 2 looks similar to the mechanism previously reported by Nikbin et al. for the dehydration of the Diels–Alder cycloadduct of DMF and ethylene catalyzed alkali-exchanged Y zeolites using mechanically embedded QM/MM calculations,[42] there is a difference in the structure of state **6**. Nikbin et al. suggest that the oxygen atom participating in the ring-opening step shown in transition state TS-**5** attacks the adjacent sp^2 hybridized carbon atom in the ring when the C–O bond cleavage occurs; therefore, it produces an epoxide intermediate instead of the alkoxide shown in state **6**. However, because an intrinsic reaction coordinate calculation starting from transition state TS-**5** ends up with the alkoxide shown in state **6**, we conclude that it is the product of ring-opening of the cycloadduct of HMFA and ethylene in Sn-BEA. This difference reflects different properties of the diene (HMFA vs DMF) because we found the epoxide intermediate in the Diels–Alder dehydration of DMF and ethylene catalyzed by Zr-BEA (Figure S1). This reaction will be discussed in the next subsection of Comparison of Catalyzed and Uncatalyzed Pathways.

Because the production of HMBA from HMFA and ethylene is a multistep process, the rate-limiting step and the apparent energy barrier of the catalytic cycle has to be determined via a kinetic analysis. We analyzed the mechanism shown in Figure 2 using the procedure suggested by Kozuch and Shaik[43,44] (see Text S3 in Supporting Information for the details of this analysis) and found that the turnover frequency (TOF) for the catalytic cycle can be described by

$$\mathrm{TOF} = \frac{k_B T}{h} e^{-\Delta G_{2,0}/RT} \quad (2)$$

where $\Delta G_{2,0}$ is the free energy difference between the transition state TS-**2** and the state **0**. This result suggests that even though there are many intermediates and transition states involved in

DOI: 10.1021/acscatal.6b01160
ACS Catal. 2016, 6, 5052–5061

Table 3. Apparent Energy and Free Energy Barriers (Energies of Transition States with respect to Solvated Reactants) of the Diels–Alder Cycloaddition in Dioxane, Si-BEA, Sn-BEA, and Zr-BEA[a]

	HMFA + ET (dioxane)	HMFA + ET (Si-BEA)	HMFA + ET (Sn-BEA)	HMFA + ET (Zr-BEA)	DMF + ET (dioxane)	DMF + ET (Zr-BEA)
E	26.3	13.0	3.2	2.9	27.0	7.7
G	42.8	51.3	41.7	40.3	42.9	42.8

[a]Numbers are reported in kcal/mol.

the mechanism shown in Figure 2, the overall kinetics of the catalytic cycle are governed by a single step, and the apparent energy barrier for the catalytic cycle is the energy difference between the transition state for the Diels–Alder reaction and the solvated reactants. Therefore, we conclude that the Diels–Alder reaction is rate-limiting for the formation of HMBA from HMFA and ethylene in Sn-BEA.

Comparison of Catalyzed and Uncatalyzed Pathways. The energy and free energy surfaces for the formation of HMBA from HMFA and ethylene in dioxane are shown in Figure 4. This solution-phase mechanism is similar to the

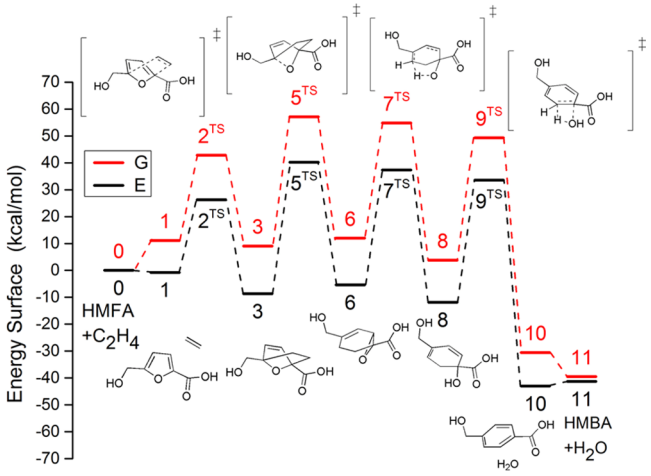

Figure 4. Energy (E) and free energy (G) surfaces for the formation of HMBA from HMFA and ethylene in dioxane.

mechanism discussed above for Sn-BEA with only a difference in the structure of state **6**. In the solution, because of the absence of electrostatic stabilization from the zeolite, this epoxide intermediate is more stable than the alkoxide form shown in Figure 2. All the intermediates and transition state species in dioxane are higher in energies than in Sn-BEA. For the Diels–Alder reaction (TS-**2**), the transition state is 23 kcal/mol lower in energies in Sn-BEA than in dioxane. For the dehydration reaction (TS-**5**, TS-**7**, and TS-**9**), the transition states in Sn-BEA are at least 40 kcal/mol lower in energies than in dioxane.

As listed in Table 3, we also considered the Diels–Alder reaction for the Si site and found that the energy and free energy barriers for Si are both much higher than Sn, suggesting that the Diels–Alder cycloaddition between HMFA and ethylene preferentially occurs on the Sn site instead of the Si sites in the pores of the zeolite. On the other hand, though the energy barrier in Sn-BEA is much lower than the one for the reaction occurring in dioxane, the free energy barrier in Sn-BEA is only slightly lower than the solution-phase barrier because of the entropy loss due to adsorption of HMFA and ethylene in the zeolite. We note that the harmonic oscillator-based approximation employed in this work can significantly overestimate the entropy loss upon adsorption because it does not account for the translational entropies of the adsorbates in zeolites.[37,38] As discussed in Text S2 in the Supporting Information, we found that the translational entropy can contribute up to −10 kcal/mol to the free energy of the adsorbed species. Therefore, the difference between the free energy barriers in Sn-BEA and dioxane is likely to increase if the translational entropy of the reactants in the zeolite is accurately taken into account.

To determine whether the Diels–Alder cycloaddition occurs in the solution or on the Sn site, one can carry out a kinetic analysis using the rates determined by the free energy barriers. However, because there is a large uncertainty associated with adsorption entropy calculations as discussed above, a direct comparison of the calculated reaction rates is likely to be problematical. An alternative approach to distinguish these two pathways is to compare the calculated energy barriers with the activation energy measured by experiments, because the Diels–Alder reaction is rate-limiting and the energy barriers in the solution and zeolites are very different. Though, to date, no one has reported an experimental activation energy for the Diels–Alder/dehydration of HMFA and ethylene, Pacheco et al. have reported the apparent activation energy for the Diels–Alder/dehydration of DMF and ethylene catalyzed by Zr-BEA.[45] For this reason, we calculated the reaction of DMF and ethylene in Zr-BEA as we did for HMFA and ethylene and found these two reactions to be similar in many aspects (see Figure S1 and Table S2 for the energy and free energy surfaces for the reaction of DMF and ethylene). A kinetic analysis confirms that the Diels–Alder reaction is also rate-limiting for the Diels–Alder/dehydration of DMF and ethylene and the apparent energy barrier for the catalytic cycle is the energy difference between the transition state for the Diels–Alder reaction and the solvated reactants, no matter whether the Diels–Alder reaction takes place in the solution or in Zr-BEA (see Text S4 in Supporting Information for the details of this analysis). Therefore, as listed in Table 3, if the Diels–Alder reaction of DMF and ethylene occurred in dioxane, one would expect the experimentally measured activation energy to be 27 kcal/mol. This, however, is not the case. What Pacheco et al. report is that for Zr-BEA, the activation energy is 8.2 kcal/mol (443–503 K).[45] On the other hand, the barrier we calculated for the Diels–Alder reaction for the Zr site is 7.7 kcal/mol, which agrees well with the experimentally measured value, suggesting that the Diels–Alder reaction of DMF and ethylene is mediated by the Zr sites.

As listed in Table 3, though the barrier for the Diels–Alder reaction of HMFA and ethylene is very close to that of DMF and ethylene in dioxane, the barrier for HMFA and ethylene is lower than DMF and ethylene on the Zr site due to better stabilization of HMFA in the zeolite because of the carboxyl and hydroxyl groups associated with this compound (this point is discussed in detail in the subsection entitled Comparison of

DOI: 10.1021/acscatal.6b01160
ACS Catal. 2016, 6, 5052–5061

Sn/Zr/Ti Activities). Therefore, the Diels–Alder reaction of HMFA and ethylene should occur on the Zr site just as the reaction of DMF and ethylene. Moreover, because the calculated barriers for the Diels–Alder reaction for Sn and Zr sites are very close to each other, the conclusions made for Zr-BEA are expected to also hold for Sn-BEA. Therefore, if the Diels–Alder reaction occurs preferentially on the Zr site instead of in solution, this should also be the case for the Sn site.

Comparison of Pathways for Diels–Alder Cycloaddition on Sn Site. In solution-phase Diels–Alder chemistry,[46] Lewis catalysis typically (normal electron demand) proceeds by coordination to the dienophile, leading to increased electron deficiency, which in turn lowers the energy of the dienophile LUMO and increases reaction rates. Inverse electron demand in which catalysis proceeds through the diene is also possible when electron-withdrawing groups are attached to the diene and electron-donating groups are attached to the dienophile. For the case of HMFA and ethylene, as shown in Figure 5, the energy gap between the diene LUMO and the dienophile HOMO is smaller than that for the typical normal electron demand case of butadiene (BD) and ethylene because in HMFA the furan oxygen and carboxylic acid group are electron-withdrawing. Because better energy matching between the diene LUMO and the dienophile HOMO implies the possibility of inverse electron demand, for the Diels–Alder cycloaddition of HMFA and ethylene mediated by Sn-BEA, the nature of the catalysis must be investigated by exploring all possibilities.

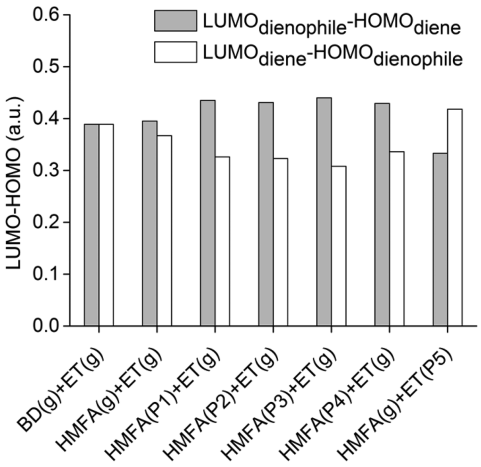

Figure 5. HOMO–LUMO gaps between the dienophile (ethylene) and the diene (butadiene or HMFA) in gas phase (g) and in the different coordination modes shown in Figure 3 (P1 to P5) calculated at ωB97X-D/Def2-TZVPD level of theory. The HOMO and LUMO in this figure refer to the proper symmetry highest-occupied and lowest-unoccupied molecular orbitals that are relevant to the Diels–Alder reaction. As shown in Figure S3 in Supporting Information, these orbitals are not necessarily to be the HOMO and LUMO of the substrate–catalyst complex.

The five mechanisms we investigated are shown in Figure 3, including four pathways starting with binding HMFA to the site by coordinating different oxygen atoms to the Sn center (P1 to P4) as well as one pathway starting with binding ethylene to the active site (P5). As shown in Figure 5, the tendency toward inverse electron demand is increased in all but one of the scenarios. The one in which ethylene, the dienophile, directly interacts with the Lewis acid site increases electron deficiency of the dienophile which in turn lowers the energy of the dienophile LUMO and strengthens the normal electron demand. Figure 5 also shows that though in pathway P5 the electron demand is enhanced in the opposite direction of the gas-phase reaction, P5 should not be particularly unfavorable because the energy gap between the frontier molecular orbitals (FMO) which are responsible for the reaction in P5 ($LUMO_{dienophile}$–$HOMO_{diene}$) is close to those in P1 to P4 ($LUMO_{diene}$–$HOMO_{dienophile}$). However, we found that P1 to P4 are actually much preferred compared to P5 because, as listed in Table 2, the apparent energy barrier for P5 is much higher than P1 to P4. This finding suggests that though analyzing the energies of FMO of reactants often provides useful insights in Diels–Alder reactions,[47] it is inadequate to explain the preference of the pathways considered. The reason for that is because the above FMO analysis only assesses the covalent interactions between the diene and the dienophile. However, because the apparent energy barrier is the energy difference between the transition state for the Diels–Alder reaction with respect to solvated reactants as discussed above, the interactions between the addends and the catalyst have to be taken into account in order to rationalize the preference of the pathways. Moreover, as will be shown below in the energy decomposition analysis, electrostatic interactions, instead of covalent interactions, govern the variations in energy barriers, so that it is actually not suitable to analyze the energy barriers of P1 to P5 using FMO theory.

Hoping to understand the variations in the energy barriers, we carried out an energy decomposition analysis.[8] This analysis starts by representing the energy of the substrate–catalyst complex in state i as the summation of energies of the substrates and catalyst and the energy change due to interactions between substrates and catalyst in state i, $\Delta E_{int}{}^{i}$, which can then be decomposed into physically relevant components as shown in eq 3

$$\begin{aligned} E(\mathrm{S{\cdot}C})^{i} &= E(\mathrm{ET}) + E(\mathrm{HMFA}) + E(\mathrm{C}) + \Delta E_{int}{}^{i} \\ &= E(\mathrm{ET}) + E(\mathrm{HMFA}) + E(\mathrm{C}) + E_{GD}{}^{i} + E_{FRZ}{}^{i} + E_{POL}{}^{i} \\ &+ E_{CT}{}^{i} = E(\mathrm{ET}) + E(\mathrm{HMFA}) + E(\mathrm{C}) + E_{GD}{}^{i} + E_{e}{}^{i} + E_{CT}{}^{i} \end{aligned} \quad (3)$$

where $E_{GD}{}^{i}$ is the energy penalty associated with geometric distortions of the isolated catalyst and reactants from their optimized geometries to the geometries that they have in state i; $E_{FRZ}{}^{i}$ is the permanent electrostatic plus exchange repulsion interaction in state i without any relaxation of the MOs; $E_{POL}{}^{i}$ and $E_{CT}{}^{i}$ are the energy lowering due to the relaxation of the frozen MOs and dative charge transfer effects in state i, respectively; and $E_{e}{}^{i}$ is the total electrostatic interaction in state i, which is the summation of $E_{FRZ}{}^{i}$ and $E_{POL}{}^{i}$. By substituting eq 3 into eq 1, the apparent energy barrier can be written as

$$\begin{aligned} E_{a} &= E(\mathrm{S{\cdot}C})^{\ddagger} - E(\mathrm{C}) - E_{sol}(\mathrm{HMFA}) - E_{sol}(\mathrm{ET}) \\ &= E_{GD}{}^{\ddagger} + E_{e}{}^{\ddagger} + E_{CT}{}^{\ddagger} - \Delta E_{sol}(\mathrm{HMFA}) - \Delta E_{sol}(\mathrm{ET}) \end{aligned} \quad (4)$$

The superscript ‡ shown in eq 4 will be ignored from this point to simplify the notation: henceforth the GD, e, and CT components refer implicitly to the transition structure.

The components comprising the Diels–Alder energy barriers for pathways P1 to P5 are depicted in Figure 6a. The magnitude of ΔE_{sol}(HMFA) and ΔE_{sol}(ET) are not shown because they are constants and do not contribute to variations

DOI: 10.1021/acscatal.6b01160
ACS Catal. 2016, 6, 5052–5061

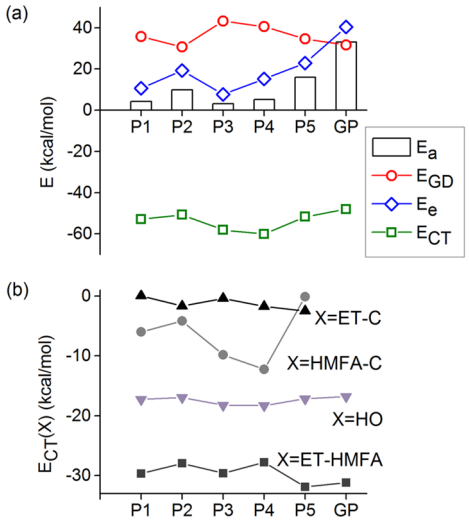

Figure 6. Energy decomposition analysis for Diels–Alder cycloaddition of HMFA and ethylene following the five different pathways whose transition states were shown in Figure 3 and in the gas phase (GP). The connecting lines are drawn only to guide the eye. The first panel, (a), shows the contributions of geometric distortion (GD), electrostatic interactions (e), and charge transfer (CT) to the total activation energy. Relative to GP, the zeolite most strongly stabilizes electrostatics, rather than CT, even for pathway P5. The second panel, (b), shows the contributions to CT from each pairwise interaction between ethylene, HMFA, and the catalyst (C), as well as the remaining higher order (HO) term, which is not pairwise additive. The dominant CT interaction is between ET and HMFA, which is only slightly enhanced in pathway P5, with a more than compensating reduction in HMFA-C interactions in P5.

in E_a. The gas-phase energy barrier for Diels–Alder reaction of HMFA and ethylene was also calculated and is designated as pathway GP in Figure 6. This gas-phase energy barrier corresponds to an imaginary process in which after HMFA and ethylene come out from the solution, the Diels–Alder cycloaddition occurs in the gas phase, rather than in the zeolite. Due to the absence of catalyst, the gas-phase energy barrier is much higher than those for pathways P1 to P5. Interestingly, Figure 6a shows that though the energy barrier for pathway P5 is lower than the gas-phase energy barrier, E_{CT} for pathway P5 is only slightly greater than the gas-phase value, indicating that in pathway P5, overall charge transfer is not significantly facilitated by the catalyst.

Seeking more insight into the charge transfer interactions in the transition structure, we further decomposed E_{CT} into the contributions from each pair of fragments[8]

$$E_{CT} = \sum_{A,B} [E_{CT}(A \rightarrow B) + E_{CT}(B \rightarrow A)] + E_{CT}(HO)$$
$$= \sum_{A,B} [E_{CT}(A{-}B)] + E_{CT}(HO) \quad (5)$$

where $E_{CT}(A \rightarrow B)$ and $E_{CT}(B \rightarrow A)$ are energy lowering due to forward and backward donations between fragments A and B calculated by the single noniterative Roothaan step; $E_{CT}(HO)$ is the contribution of higher order relaxation effects; and $E_{CT}(A{-}B)$ is the total charge transfer interaction between fragments A and B, which is the summation of $E_{CT}(A \rightarrow B)$ and $E_{CT}(B \rightarrow A)$.

It is shown in Figure 6b that the contribution of charge transfer interactions between ethylene and the catalyst, $E_{CT}(ET{-}C)$, is close to zero for all pathways, including the one in which ethylene is directly placed on top of the site (P5), suggesting that the Lewis acid site has very limited ability to draw electrons away from ethylene. On the contrary, the contribution of charge transfer interactions between HMFA and the catalyst, $E_{CT}(HMFA{-}C)$, varies significantly by pathway. Unsurprisingly, the P5 transition structure does not favor charge transfers between HMFA and the catalyst. As shown in Figure 6b, $E_{CT}(HMFA{-}C)$ for pathway P5 is significantly lower than pathways P1 to P4, in which HMFA is assumed to bind directly to active sites. Therefore, as shown in Figure 6a, pathway P5 does not favor charge transfer interactions comparing with pathways P1 to P4.

Interestingly, Figure 6b shows that for pathways P1 to P5, none of the values of $E_{CT}(ET{-}HMFA)$ are significantly larger than pathway GP, suggesting that the Diels–Alder electron transfers induced by the catalyst are actually very small for all the pathways. This finding is consistent with the experimental observation reported very recently for DMF and ethylene that Sn-, Zr-, and Ti-BEA are only slightly more active to catalyze the Diels–Alder reaction comparing with H-BEA,[48] a Brønsted acid zeolite which is not effective to increase the intrinsic rate of the Diels–Alder reaction.[7] However, this result is unexpected in the above analysis of energies of frontier molecular orbitals, most likely because in the transition structure, the frontier molecular orbitals of HMFA and ethylene overlap better in the gas phase than in the zeolite so that even though the energy gaps between the frontier molecular orbitals are decreased by the catalyst, the charge transfer interactions between the reactants are not significantly enhanced.

Figure 6a shows that the net values of total electrostatic and exchange repulsion interactions in the transition structure, E_e, are positive for all the scenarios, suggesting that electron distributions of each fragment overlap significantly in the transition states for the pathways considered. Moreover, we found that though all three components of the energy barriers, E_{GD}, E_e, and E_{CT}, vary with pathway, the variations in energy barriers are mainly governed by E_e because E_{GD} and E_{CT} have a net effect that is roughly the same for all pathways. For instance, the value of E_e for pathway GP is much higher than those occurring in zeolites due to the absence of electrostatic stabilizations from the active site and extended zeolite environment, so that the highest energy barrier is for the gas phase reaction.

For the pathways mediated by the Sn site (P1 to P5), we found that the magnitude of E_e correlates quite well with the dipole moment on the substrate molecule that directly interacts with the active site, as shown in Figure 7. This can be rationalized by considering the electrostatic interaction between the active site and the HMFA-ethylene complex formed in the transition state. If the component of the complex close to the active site carries a strong dipole moment, the electrostatic stabilization between the complex and the active site is strong so that the positive value of E_e caused by electron–electron repulsions is decreased. Therefore, the lowest values of E_e and E_a are for pathway P3, in which the substrate directly interacting with the site in the transition state carried the strongest dipole moment. This finding also explains why pathway P5, the scenario in which ethylene interacts directly with the active site is not preferred. As shown in Figure 7, because the dipole moment on ethylene in the transition state is much smaller than that on HMFA, the value of E_e for

DOI: 10.1021/acscatal.6b01160
ACS Catal. 2016, 6, 5052–5061

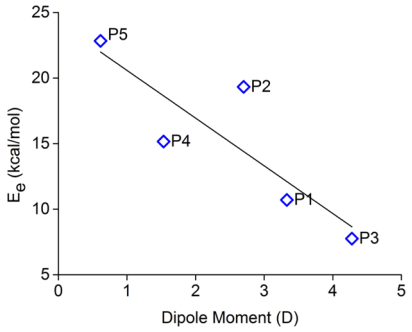

Figure 7. Correlation between the total electrostatic interactions and the dipole moment on the substrate which directly interacts with the active site (HMFA for pathways P1 to P4 and ethylene for pathway P5).

pathway P5 is significantly higher than other pathways, resulting in high E_a for pathway P5.

Comparison of Sn/Zr/Ti Activities. To investigate how substitution of the heteroatom affects catalyst performance, the energy surface shown in Figure 2 was recalculated after replacing Sn by Zr or Ti. The energy barriers for the five Diels–Alder pathways shown in Figure 3 were also recalculated and pathway P3 was also confirmed to be the preferred pathway for Zr and Ti (see Table S6 in Supporting Information for the free energy barriers). However, following the same kinetic analysis described above, we found the rate-limiting step for Zr to be the Diels–Alder reaction (TS-**2**), whereas for Ti it shifts to the ring-opening of the cycloadduct (TS-**5**) in the dehydration process. Furthermore, as shown in Figure 8, the energy surface

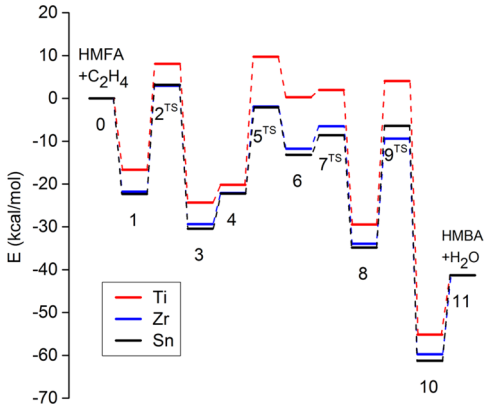

Figure 8. Energy surface for the most favorable path for formation of HMBA from HMFA and ethylene mediated by the T2 site of Sn-BEA, Zr-BEA, and Ti-BEA (mechanism shown in Figure 2). Free energy surface can be found in Supporting Information (Figure S2).

for Zr is very close to that of Sn, whereas the energy surface for Ti is significantly higher relative to those for Sn and Zr. This result agrees well with the experimental observation that the activity of Zr-BEA is comparable to Sn-BEA but is much higher than that for Ti-BEA.[6] It has been reported very recently that the same trend was observed experimentally for Meerwein–Ponndorf–Verley (MPV) reduction of methyl levulinate to γ-valerolactone,[49] though the MPV and the present reaction are quite different in nature. This trend is also consistent with the results reported previously in two independent DFT studies that the calculated energy barriers for the isomerization of glucose to fructose[15] and the epimerization of glucose to mannose[50] mediated by Sn-BEA and Zr-BEA are lower than that for Ti-BEA.

The difference in the activities of Sn-BEA, Zr-BEA, and Ti-BEA can be rationalized by the difference in the Lewis acidities of the active sites. Using the adsorption energies of water calculated by DFT as a gauge, Yang et al. reported that the Lewis acidities of Sn and Zr site are generally quite similar, whereas they are substantially higher than that of the Ti site.[19] However, our previous study shows that for the reactions where the activities of the Sn and Zr site are comparable, the effects that lead to this result can be different.[15] For the isomerization of glucose to fructose, it has been shown that because the Sn site has stronger partial charge separation between the Sn atom and the O atoms in the first coordination sphere, the Sn site can stabilize the transition state species electrostatically better than can the Zr site.[15] On the other hand, because the Zr atom is more polarizable than the Sn atom,[51] there is a lower energy penalty associated with geometric distortion of the Zr site from its optimized geometry to the geometry in the transition state.[15] Using energy decomposition analysis, we found similar effects here. As listed in Table 4, for the Diels–Alder reaction, though the energy barriers of the Sn and Zr site are comparable, the individual contributing factors are different: the lower geometric distortion (E_{GD}) in Zr overcomes less favorable electrostatic (E_e) and charge transfer (E_{CT}) effects. The more favorable electrostatic and charge transfer interactions for the Sn site can be explained by the larger positive charge located on the central atom (Q_M) of the Sn site. On the other hand, the lower energy penalty associated with geometric distortion of the Zr site can be rationalized by the higher polarizability of Zr compared to Sn.

It should be noted that because the energy decomposition analysis can only decompose electronic energies without thermodynamic corrections, the sum of the energy components discussed in EDA is equal to the electronic energy barriers (see eq 4) and deviates slightly from the reported energy barriers, which are thermodynamically corrected values.

CONCLUSIONS

Detailed mechanisms for the formation of HMBA from HMFA and ethylene in Sn-BEA and the associated energy surfaces have been obtained using QM/MM simulations. The formation of HMBA consists of a Diels–Alder cycloaddition, which is rate-limiting, followed by Lewis acid-catalyzed dehydration (see Figure 2). Compared with the solution-phase reaction in

Table 4. Apparent Energy Barriers (Energies of Transition States with respect to Solvated Reactants) and Energy Decomposition Analysis for Diels–Alder Reaction (P3) Mediated by Sn and Zr Sites

	E_a (kcal/mol)	E_{GD} (kcal/mol)	E_e (kcal/mol)	E_{CT} (kcal/mol)	Q_M[a] (a.u.)	α[b] (10^{-24} cm^3)
Sn	3.2	43.3	7.8	−58.1	2.7	7.8
Zr	2.9	37.4	10.2	−54.5	2.4	17.9

[a]Partial charge associated with the central atom of the active site. [b]Polarizability of the heteroatom contained in the active site, ref 51.

DOI: 10.1021/acscatal.6b01160
ACS Catal. 2016, 6, 5052–5061

dioxane, all the intermediates are more energetically favorable in Sn-BEA. Six possible pathways have been investigated for the Diels–Alder cycloaddition of HMFA and ethylene in Sn-BEA, including one pathway for the Si site, four pathways starting with binding HMFA to the Sn site by coordinating different oxygen atoms of HMFA to the Sn atom, and one pathway starting with binding ethylene to the Sn site (see Figure 3). The energy decomposition analysis shows that though Sn-BEA is a Lewis acid zeolite, it does not significantly facilitate charge transfer between HMFA and ethylene. On the contrary, compared to Diels–Alder cycloaddition of HMFA and ethylene occurring in gas phase, we found that the predominant effect that decreases the energy barrier on Sn-BEA is electrostatic stabilization by the catalyst. The magnitude of the electrostatic stabilization is strongly affected by the dipole moments on the substrate molecule which interacts directly with the active site in the transition state. Therefore, instead of binding ethylene to the Sn site (as in Lewis acid catalysis with normal electron demand), configurations in which HMFA binds to the Sn site are preferred. The coordination mode that maximizes the dipole moment on HMFA in the transition state for Diels–Alder cycloaddition is to coordinate the oxygen atom of the carbonyl group of HMFA to the Sn atom; therefore, the mechanism starts with binding HMFA to the site in this coordination mode is the preferred pathway for Diels–Alder cycloaddition of HMFA and ethylene in Sn-BEA.

The effect of the identity of the active site atom on activity was investigated by substituting Sn with Zr and Ti. The energy barriers for the Sn and Zr sites are the lowest, in good agreement with experimental observation that the activity of Zr-BEA is comparable with Sn-BEA and is much higher than Ti-BEA. Using energy decomposition analysis, it is shown that the reasons for activity at Sn and Zr sites differ. For the Sn site, the central atom of the site carries a high positive charge so that the favorable electrostatic and charge transfer interactions between the substrates and the site stabilize the transition state. On the other hand, comparing with Sn site, Zr site has lower energy penalty associated with geometric distortion from its resting geometry to the geometry in the transition state because Zr is more polarizable than Sn; therefore, the energy barrier for Zr site is comparable with Sn site even though the electrostatic and charge transfer interactions for the Zr site are less favorable than for the Sn site.

■ ASSOCIATED CONTENT

Supporting Information

The Supporting Information is available free of charge on the ACS Publications website at DOI: 10.1021/acscatal.6b01160.

Additional information as noted in the text, including kinetic analysis, free energy data, HOMO and LUMO that are relevant to the Diels–Alder reaction, and a discussion of the local flexibility of the lattice (PDF)

■ AUTHOR INFORMATION

Corresponding Author

*E-mail: alexbell@berkeley.edu.

Notes

The authors declare no competing financial interest.

■ ACKNOWLEDGMENTS

This work was supported by the XC^2 program funded by BP. M.H.G. acknowledges additional support from the U.S. National Science Foundation (Grant CHE- 1363342).

■ REFERENCES

(1) Wantanachaisaeng, P.; O'Neil, K.*Capturing Opportunities for Para-Xylene Production*; Technical Report; UOP: A Honeywell Company: Des Plaines, IL, 2010.

(2) Williams, C. L.; Chang, C.-C.; Do, P.; Nikbin, N.; Caratzoulas, S.; Vlachos, D. G.; Lobo, R. F.; Fan, W.; Dauenhauer, P. J. *ACS Catal.* **2012**, *2*, 935–939.

(3) Zhang, M.; Yu, Y. *Ind. Eng. Chem. Res.* **2013**, *52*, 9505–9514.

(4) Román-Leshkov, Y.; Barrett, C. J.; Liu, Z. Y.; Dumesic, J. A. *Nature* **2007**, *447*, 982–985.

(5) Lin, Z.; Nikolakis, V.; Ierapetritou, M. *Ind. Eng. Chem. Res.* **2014**, *53*, 10688–10699.

(6) Pacheco, J. J.; Davis, M. E. *Proc. Natl. Acad. Sci. U. S. A.* **2014**, *111*, 8363–8367.

(7) Li, Y.-P.; Head-Gordon, M.; Bell, A. T. *J. Phys. Chem. C* **2014**, *118*, 22090–22095.

(8) Khaliullin, R. Z.; Cobar, E. A.; Lochan, R. C.; Bell, A. T.; Head-Gordon, M. *J. Phys. Chem. A* **2007**, *111*, 8753–8765.

(9) Roy, S.; Bakhmutsky, K.; Mahmoud, E.; Lobo, R. F.; Gorte, R. J. *ACS Catal.* **2013**, *3*, 573–580.

(10) Gunther, W. R.; Michaelis, V. K.; Caporini, M. A.; Griffin, R. G.; Román-Leshkov, Y. *J. Am. Chem. Soc.* **2014**, *136*, 6219–6222.

(11) Boronat, M.; Concepción, P.; Corma, A.; Renz, M.; Valencia, S. *J. Catal.* **2005**, *234*, 111–118.

(12) Wolf, P.; Valla, M.; Rossini, A. J.; Comas-Vives, A.; Núñez-Zarur, F.; Malaman, B.; Lesage, A.; Emsley, L.; Copéret, C.; Hermans, I. *Angew. Chem., Int. Ed.* **2014**, *53*, 10179–10183.

(13) Boronat, M.; Corma, A.; Renz, M. *J. Phys. Chem. B* **2006**, *110*, 21168–21174.

(14) Bermejo-Deval, R.; Assary, R. S.; Nikolla, E.; Moliner, M.; Román-Leshkov, Y.; Hwang, S.-J.; Palsdottir, A.; Silverman, D.; Lobo, R. F.; Curtiss, L. A.; Davis, M. E. *Proc. Natl. Acad. Sci. U. S. A.* **2012**, *109*, 9727–9732.

(15) Li, Y.-P.; Head-Gordon, M.; Bell, A. T. *ACS Catal.* **2014**, *4*, 1537–1545.

(16) Newsam, J. M.; Treacy, M. M. J.; Koetsier, W. T.; Gruyter, C. B. D. *Proc. R. Soc. London, Ser. A* **1988**, *420*, 375–405.

(17) Bare, S. R.; Kelly, S. D.; Sinkler, W.; Low, J. J.; Modica, F. S.; Valencia, S.; Corma, A.; Nemeth, L. T. *J. Am. Chem. Soc.* **2005**, *127*, 12924–12932.

(18) Shetty, S.; Pal, S.; Kanhere, D.; Goursot, A. *Chem. - Eur. J.* **2005**, *12*, 518–523.

(19) Yang, G.; Pidko, E. A.; Hensen, E. J. M. *J. Phys. Chem. C* **2013**, *117*, 3976–3986.

(20) Zimmerman, P. M.; Head-Gordon, M.; Bell, A. T. *J. Chem. Theory Comput.* **2011**, *7*, 1695–1703.

(21) Janda, A.; Vlaisavljevich, B.; Lin, L.-C.; Mallikarjun Sharada, S.; Smit, B.; Head-Gordon, M.; Bell, A. T. *J. Phys. Chem. C* **2015**, *119*, 10427–10438.

(22) Li, Y.-P.; Gomes, J.; Mallikarjun Sharada, S.; Bell, A. T.; Head-Gordon, M. *J. Phys. Chem. C* **2015**, *119*, 1840–1850.

(23) Gomes, J.; Head-Gordon, M.; Bell, A. T. *J. Phys. Chem. C* **2014**, *118*, 21409–21419.

(24) Mallikarjun Sharada, S.; Zimmerman, P. M.; Bell, A. T.; Head-Gordon, M. *J. Phys. Chem. C* **2013**, *117*, 12600–12611.

(25) Zimmerman, P. M.; Tranca, D. C.; Gomes, J.; Lambrecht, D. S.; Head-Gordon, M.; Bell, A. T. *J. Am. Chem. Soc.* **2012**, *134*, 19468–19476.

(26) Gomes, J.; Zimmerman, P. M.; Head-Gordon, M.; Bell, A. T. *J. Phys. Chem. C* **2012**, *116*, 15406–15414.

(27) Mlinar, A. N.; Zimmerman, P. M.; Celik, F. E.; Head-Gordon, M.; Bell, A. T. *J. Catal.* **2012**, *288*, 65–73.

DOI: 10.1021/acscatal.6b01160
ACS Catal. 2016, 6, 5052–5061

(28) Foloppe, N.; MacKerell, A. D., Jr. *J. Comput. Chem.* **2000**, *21*, 86−104.
(29) Yin, D.; MacKerell, A. D. *J. Comput. Chem.* **1998**, *19*, 334−348.
(30) Vanommeslaeghe, K.; Hatcher, E.; Acharya, C.; Kundu, S.; Zhong, S.; Shim, J.; Darian, E.; Guvench, O.; Lopes, P.; Vorobyov, I.; Mackerell, A. D. *J. Comput. Chem.* **2010**, *31*, 671−690.
(31) Chai, J.-D.; Head-Gordon, M. *Phys. Chem. Chem. Phys.* **2008**, *10*, 6615−6620.
(32) Chai, J.-D.; Head-Gordon, M. *J. Chem. Phys.* **2008**, *128*, 084106−084115.
(33) Behn, A.; Zimmerman, P. M.; Bell, A. T.; Head-Gordon, M. *J. Chem. Phys.* **2011**, *135*, 224108.
(34) Shao, Y.; Gan, Z.; Epifanovsky, E.; Gilbert, A. T. B.; Wormit, M.; Kussmann, J.; Lange, A. W.; Behn, A.; Deng, J.; Feng, X.; Ghosh, D.; Goldey, M.; Horn, P. R.; Jacobson, L. D.; Kaliman, I.; Khaliullin, R. Z.; Kuś, T.; Landau, A.; Liu, J.; Proynov, E. I.; Rhee, Y. M.; Richard, R. M.; Rohrdanz, M. A.; Steele, R. P.; Sundstrom, E. J.; Woodcock, H. L.; Zimmerman, P. M.; Zuev, D.; Albrecht, B.; Alguire, E.; Austin, B.; Beran, G. J. O.; Bernard, Y. A.; Berquist, E.; Brandhorst, K.; Bravaya, K. B.; Brown, S. T.; Casanova, D.; Chang, C.-M.; Chen, Y.; Chien, S. H.; Closser, K. D.; Crittenden, D. L.; Diedenhofen, M.; DiStasio, R. A.; Do, H.; Dutoi, A. D.; Edgar, R. G.; Fatehi, S.; Fusti-Molnar, L.; Ghysels, A.; Golubeva-Zadorozhnaya, A.; Gomes, J.; Hanson-Heine, M. W. D.; Harbach, P. H. P.; Hauser, A. W.; Hohenstein, E. G.; Holden, Z. C.; Jagau, T.-C.; Ji, H.; Kaduk, B.; Khistyaev, K.; Kim, J.; Kim, J.; King, R. A.; Klunzinger, P.; Kosenkov, D.; Kowalczyk, T.; Krauter, C. M.; Lao, K. U.; Laurent, A. D.; Lawler, K. V.; Levchenko, S. V.; Lin, C. Y.; Liu, F.; Livshits, E.; Lochan, R. C.; Luenser, A.; Manohar, P.; Manzer, S. F.; Mao, S.-P.; Mardirossian, N.; Marenich, A. V.; Maurer, S. A.; Mayhall, N. J.; Neuscamman, E.; Oana, C. M.; Olivares-Amaya, R.; O'Neill, D. P.; Parkhill, J. A.; Perrine, T. M.; Peverati, R.; Prociuk, A.; Rehn, D. R.; Rosta, E.; Russ, N. J.; Sharada, S. M.; Sharma, S.; Small, D. W.; Sodt, A.; Stein, T.; Stück, D.; Su, Y.-C.; Thom, A. J. W.; Tsuchimochi, T.; Vanovschi, V.; Vogt, L.; Vydrov, O.; Wang, T.; Watson, M. A.; Wenzel, J.; White, A.; Williams, C. F.; Yang, J.; Yeganeh, S.; Yost, S. R.; You, Z.-Q.; Zhang, I. Y.; Zhang, X.; Zhao, Y.; Brooks, B. R.; Chan, G. K. L.; Chipman, D. M.; Cramer, C. J.; Goddard, W. A.; Gordon, M. S.; Hehre, W. J.; Klamt, A.; Schaefer, H. F.; Schmidt, M. W.; Sherrill, C. D.; Truhlar, D. G.; Warshel, A.; Xu, X.; Aspuru-Guzik, A.; Baer, R.; Bell, A. T.; Besley, N. A.; Chai, J.-D.; Dreuw, A.; Dunietz, B. D.; Furlani, T. R.; Gwaltney, S. R.; Hsu, C.-P.; Jung, Y.; Kong, J.; Lambrecht, D. S.; Liang, W.; Ochsenfeld, C.; Rassolov, V. A.; Slipchenko, L. V.; Subotnik, J. E.; Van Voorhis, T.; Herbert, J. M.; Krylov, A. I.; Gill, P. M. W.; Head-Gordon, M. *Mol. Phys.* **2015**, *113*, 184−215.
(35) Foster, J. P.; Weinhold, F. *J. Am. Chem. Soc.* **1980**, *102*, 7211−7218.
(36) Grimme, S. *Chem. - Eur. J.* **2012**, *18*, 9955−9964.
(37) De Moor, B. A.; Reyniers, M.-F.; Gobin, O. C.; Lercher, J. A.; Marin, G. B. *J. Phys. Chem. C* **2011**, *115*, 1204−1219.
(38) Piccini, G.; Sauer, J. *J. Chem. Theory Comput.* **2014**, *10*, 2479−2487.
(39) Cossi, M.; Rega, N.; Scalmani, G.; Barone, V. *J. Comput. Chem.* **2003**, *24*, 669−681.
(40) Vaitheeswaran, S.; Green, S. K.; Dauenhauer, P.; Auerbach, S. M. *ACS Catal.* **2013**, *3*, 2012−2019.
(41) Xu, L.; Jiang, Y.; Yao, Q.; Han, Z.; Zhang, Y.; Fu, Y.; Guo, Q.; Huber, G. W. *Green Chem.* **2015**, *17*, 1281−1290.
(42) Nikbin, N.; Feng, S.; Caratzoulas, S.; Vlachos, D. G. *J. Phys. Chem. C* **2014**, *118*, 24415−24424.
(43) Kozuch, S.; Shaik, S. *J. Am. Chem. Soc.* **2006**, *128*, 3355−3365.
(44) Kozuch, S.; Shaik, S. *Acc. Chem. Res.* **2011**, *44*, 101−110.
(45) Pacheco, J. J.; Labinger, J. A.; Sessions, A. L.; Davis, M. E. *ACS Catal.* **2015**, *5*, 5904−5913.
(46) Houk, K. N.; Strozier, R. W. *J. Am. Chem. Soc.* **1973**, *95*, 4094−4096.
(47) Houk, K. N. *Acc. Chem. Res.* **1975**, *8*, 361−369.
(48) Chang, C.-C.; Cho, H. J.; Yu, J.; Gorte, R. J.; Gulbinski, J.; Dauenhauer, P.; Fan, W. *Green Chem.* **2016**, *18*, 1368−1376.
(49) Luo, H. Y.; Consoli, D. F.; Gunther, W. R.; Román-Leshkov, Y. *J. Catal.* **2014**, *320*, 198−207.
(50) Chethana, B. K.; Mushrif, S. H. *J. Catal.* **2015**, *323*, 158−164.
(51) *CRC Handbook of Chemistry and Physics*, 93rd ed. (Internet Version); Haynes, W. M., Ed.; CRC Press/Taylor and Francis: Boca Raton, FL, 2013.

DOI: 10.1021/acscatal.6b01160
ACS Catal. 2016, 6, 5052−5061